

Characteristics of colliding sea breeze gravity current fronts: a laboratory study

Karin van der Wiel^{ab*}, Sarah T. Gille^c, Stefan G. Llewellyn Smith^{c,d}, P. F. Linden^e and Claudia Cenedese^f

^aCentre for Ocean and Atmospheric Sciences, School of Environmental Sciences, University of East Anglia, Norwich, UK

^bAtmospheric and Oceanic Sciences, Princeton University, Princeton, NJ, USA

^cScripps Institution of Oceanography, University of California San Diego, La Jolla, CA, USA

^dDepartment of Mechanical and Aerospace Engineering, University of California San Diego, La Jolla CA, USA

^eDepartment of Applied Mathematics and Theoretical Physics, Centre for Mathematical Sciences, University of Cambridge, Cambridge, UK

^fWoods Hole Oceanographic Institution, Woods Hole, MA, USA

*Correspondence to: K. van der Wiel, e-mail: kwiel@princeton.edu

Sea and land breeze circulations driven by surface temperature differences between land and sea often evolve into gravity currents with sharp fronts. Along narrow peninsulas, islands and enclosed seas, sea/land breeze fronts from opposing shorelines may converge and collide and may initiate deep convection and heavy precipitation. Here we investigate the collision of two sea breeze gravity current fronts in an analogue laboratory setting. We examine these collisions by means of ‘lock-exchange’ experiments in a rectangular channel. The effects of differences in gravity current density and height are studied. Upon collision, a sharp front separating the two currents develops. For symmetric collisions (the same current densities and heights) this front is vertical and stationary. For asymmetric collisions (density differences, similar heights) the front is tilted, changes shape in time and propagates in the same direction as the heavier current before the collision. Both symmetric and asymmetric collisions lead to upward displacement of fluid from the gravity currents and mixing along the plane of contact. The amount of mixing along the collision front decreases with asymmetry. Height differences impact post-collision horizontal propagation: there is significant propagation in the same direction as the higher current before collision, independent of density differences. Collisions of two gravity current fronts force sustained ascending motions which increase the potential for deep convection. From our experiments we conclude that this potential is larger in stationary collision fronts from symmetric sea breeze collisions than in propagating collision fronts from asymmetric sea breeze collisions.

Key Words: sea breeze; land breeze; gravity current; convergence; deep convection; GFD; fluid dynamics

Received . . .

1. Introduction

Differences in the heating of air over the land and the sea create horizontal density differences that set up atmospheric circulations. These circulations, referred to as the sea or land breeze, occur in many coastal regions and are examples of atmospheric gravity currents. Gravity currents, or buoyancy-driven currents, are flows along a boundary driven by horizontal density differences under the influence of a gravitational field (Simpson 1997; Miller *et al.* 2003).

Sea/land breeze development is influenced by many meteorological and environmental factors, including the land-sea surface temperature difference, atmospheric stability, orography, the curvature of the local coast and large-scale meteorological conditions (Miller *et al.* 2003). Ahead of a sea breeze front ascending motions of the order $1\text{--}2\text{ m s}^{-1}$ are found (Simpson 1969; Helmis *et al.* 1987; Moncrieff & Liu 1999). The horizontal extents of sea/land breezes depend strongly on latitude, as closer to the Equator the solar insolation is stronger and the Coriolis force due to the rotation of the Earth is less (e.g. Niino 1987; Yan & Anthes 1987; Tijn *et al.* 1999; Miller *et al.* 2003). In England (50°N) and the Netherlands (52°N) sea breeze fronts have been observed 100 km inland (Simpson *et al.* 1977; Tijn *et al.* 1999), while in southern Australia (32°S) fronts can travel as far as 400 km from the coast (Clarke 1983).

These large inland penetrations mean that for narrow peninsulas or islands, sea breezes from opposing shorelines can interact. Observational case studies and numerical model experiments for locations around the world have shown that such convergences are widespread. Known examples of sea breeze convergence include: Florida, USA (Byers & Rodebush 1948; Pielke 1974; Burpee 1979; Nicholls *et al.* 1991), the Cape York Peninsula, Australia (Noonan & Smith 1986), Mallorca, Spain (Ramis *et al.* 1990; Sumner *et al.* 1993), the Tiwi islands, Australia (Carbone *et al.* 2000; Crook 2001), Salento, Italy (Mangia *et al.* 2004) and Cornwall, England (Golding 2005). Land breeze convergence has been shown to occur over the North American Great Lakes (Forbes & Merritt 1984; Niziol *et al.* 1995), between the Tiwi islands and Australia (Wapler & Lane 2012), and based on global satellite measurements Gille *et al.* (2003) show that

such convergences can be expected over any body of water narrower than 500 km. Gille & Llewellyn Smith (2014) note that for enclosed seas, wind phase lines converge at gravity-wave propagation speeds, which are faster than the propagation speeds of land breeze fronts. For convenience, we will refer to both sea and land breezes as ‘sea breezes’ in the remainder of this paper.

For sea breeze convergences, the horizontal propagation speed is probably the most important factor in determining how far inland a front travels and whether a collision will occur. This speed is most significantly influenced by (i) the magnitude of the surface temperature difference between land and sea and (ii) the strength and direction of the ambient wind (e.g. Arritt 1993; Tijn *et al.* 1999; Gahmberg *et al.* 2010; Warren 2014). In turn, the temperature difference is mostly a function of the surface sensible heat flux into the ground. Here it will be assumed that the conditions to create a collision are met, and the main focus will be on the collision event. Factors influencing the density, the propagation speed or the height of the sea breeze after its formation (e.g. Robinson *et al.* 2013) will therefore be neglected.

In operational weather forecasting, increasing the predictive skill of severe weather conditions is important. For local communities, knowing both the time and location of extreme events with substantial advance warning is crucial (Wilson *et al.* 1998; Browning *et al.* 2007; Wulfmeyer *et al.* 2011). Many previous studies on the convergence and collision of two sea breeze fronts are case studies based on either observational data or numerical experiments. Most of these studies show that these collisions lead to an enhancement of ascending motion, deep convection and precipitation (e.g. Byers & Rodebush 1948; Forbes & Merritt 1984; Blanchard & López 1985; Noonan & Smith 1986; Nicholls *et al.* 1991; Sumner *et al.* 1993; Fankhauser *et al.* 1995; Carbone *et al.* 2000; Crook 2001; Golding 2005; Wapler & Lane 2012; Warren 2014; Rizza *et al.* 2015). Sea breeze convergence may also lead to enhanced air pollution (Mangia *et al.* 2010). The timing and location of the collision and its heaviest impacts depend on many factors including the curvature of coastlines, topographic features, soil moisture levels and the presence of land breezes prior to sea breeze development (Baker *et al.* 2001).

We highlight two idealized numerical studies that have systematically investigated specific aspects of the sea breeze

80 convergence. Xian & Pielke (1991) show that maximum
81 ascending motions are triggered over land masses of 100-150
82 km width; narrower land masses do not allow the development
83 of a mature sea breeze circulation, collisions over wider land
84 masses generally occur after sunset and consequently have
85 weaker convergence. Warren (2014) shows that the collision of
86 more developed sea breezes (increased propagation speeds and
87 increased heights) displace more air mass in the vertical than
88 weaker sea breezes. Factors that are shown to impact vertical
89 air displacement, in order of influence, are: surface heat flux,
90 atmospheric mixed-layer depth and atmospheric stability. Latitude
91 and land surface roughness are shown to have less influence.
92 Furthermore, ambient wind strength and direction and coastal
93 curvature are shown to influence the strength of convergence and,
94 if a collision happens, its location.

95 Besides sea breezes, convective outflows also take the form
96 of gravity currents (Simpson 1997). Outflow currents are formed
97 by downdrafts from thunderstorms, evaporative cooling in the
98 thunderstorms creates the cold, dense air of the gravity current.
99 Collisions of two of such outflow currents, or collisions between
100 an outflow and a sea breeze front may initiate convection in a way
101 similar to collisions of two sea breeze fronts (e.g. Droegemeier
102 & Wilhelmson 1985; Wilson & Schreiber 1986; Carbone *et al.*
103 1990; Kingsmill 1995; Moncrieff & Liu 1999; Banacos & Schultz
104 2005; Soderholm *et al.* 2015).

105 In this study, we present laboratory experiments designed to
106 examine the collision of two gravity currents. Such experiments
107 provide a way to investigate these collisions in a controlled
108 setting, and to extend the knowledge from field campaigns,
109 observational, and numerical studies. There have been many
110 experimental studies on gravity currents (e.g. Britter & Simpson
111 1978; Hacker *et al.* 1996; Simpson 1997; Cenedese & Adduce
112 2008; Shin 2001; Maxworthy *et al.* 2002; Shin *et al.* 2004;
113 Dai 2013); however few previous studies have considered two
114 colliding gravity currents. Simpson (1997) showed the emergence
115 of two bores travelling in opposite directions after a collision.
116 Shin (2001) presented experimental results based on collisions of
117 currents of equal density but different heights and developed a
118 theory based on momentum and energy conservation that predicts

the propagation speed of the bores formed as a result of the
collision.

The novelty of the experiments described in this paper lies in
examining the influence of both height differences and density
differences between the colliding fronts, thus expanding on the
earlier experimental work of Shin (2001). Height and density are
two of the key parameters that vary in environmental sea breeze
convergences and which have been shown to impact the strength
of the collision (Warren 2014). In the natural environment, density
differences in sea breezes may be created by differing sea surface
temperatures on opposing coasts. In convective outflows the rate
of evaporative cooling determines the outflow density. Height
differences may be expected in the natural environment in the
collision of sea breeze fronts and convective outflows, or in the
collision of two outflow currents. We restrict the analysis to the
two-dimensional case which is relevant since many sea breeze
circulations produce relatively straight fronts. The experiments
are described in Section 2. Experimental results are illustrated in
Section 3. The conclusions are discussed in Section 4.

2. Experimental description

For this study gravity currents were created in a laboratory tank by
means of 'lock exchange' experiments, in which fluids of different
density were initially at rest and separated by a vertical barrier.
Once the barrier was removed, the denser fluid flowed along the
bottom of the tank into the lighter, ambient fluid.

The experiments were carried out in a horizontal rectangular
glass channel, 150 cm long and 15.5 cm wide (Figure 1). In all
experiments the channel was filled to a depth of $H_0 = 20$ cm. The
tank was illuminated from behind using a uniform light sheet,
and the experiments were filmed using a video camera located
approximately 2 m from the tank.

At each end of the tank a separate section, or 'lock', was made
using a vertical barrier, or 'lock gate' (dashed lines in Figure 1).
The locks were 20 cm long. In the locks salt (NaCl) was added
to the water to increase the density and thus create the horizontal
density differences needed for the gravity currents. Yellow and
blue food dyes were added to distinguish the denser fluids from the
transparent, fresh, ambient fluid. Densities were measured with

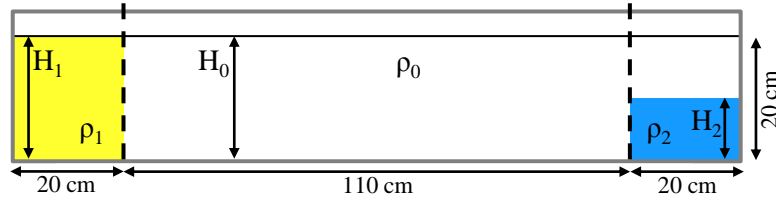


Figure 1. Sketch of the experimental setup. Symbols are defined in the text.

157 an accuracy of $5 \times 10^{-5} \text{ g cm}^{-3}$ using an Anton Paar DMA 58
158 densitometer.

159 Two sets of experiments were performed. The first set was
160 designed to study the influence of (relative) differences in density
161 on the collision. This set of experiments will be referred to
162 as ‘full-depth’ lock exchanges or ‘full-depth’ experiments. Both
163 locks were filled to the top with dense fluid, i.e. $H_1 = H_2 =$
164 H_0 , where H_1 and H_2 are the heights of denser fluids in the
165 two locks. The density in the locks are denoted by ρ_1 and ρ_2 ,
166 respectively (Figure 1). In total eighteen full-depth experiments
167 were conducted.

168 In the second set of experiments the depth of *one* of the locks
169 was half of the total depth ($H_1 = H_0, H_2 = \frac{1}{2}H_0$, Figure 1). This
170 set of experiments will be referred to as ‘half-depth’ experiments.
171 A second independent parameter, the gravity current height, was
172 introduced to the problem this way. In total fourteen half-depth
173 experiments were conducted.

174 At the beginning of each experiment, the lock gates were
175 pulled up simultaneously. The propagation speeds of the gravity
176 currents were found by image analysis of the experimental videos.
177 The position of the front was mapped in time, and a linear
178 regression line was fitted. Soon after the release, the gravity
179 currents entered the constant-speed regime (Rottman & Simpson
180 1983), and the collision event happened within this regime. The
181 Reynolds number of the currents always exceeds 3500 and thus
182 viscous effects are negligible (Simpson 1997, p. 141).

183 The dimensionless horizontal propagation speed of a gravity
184 current generated from a lock exchange is given by the Froude
185 number,

$$F_H = \frac{U}{\sqrt{g'H}}, \quad (1)$$

186 where g' is the reduced gravity, H is the height of the dense fluid in
187 the lock and U the horizontal propagation speed (Simpson 1997).
188 The reduced gravity is the buoyancy between the gravity current

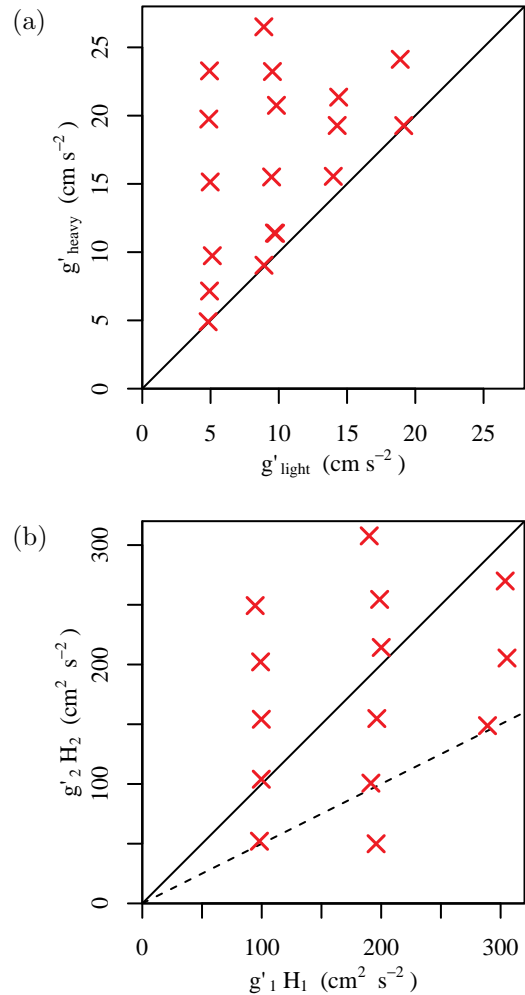


Figure 2. Positions in parameter space of the experiments. (a) Full-depth experiments, with diagonal line indicating the symmetric case in which $g'_{light} = g'_{heavy}$. (b) Half-depth experiments, with the solid diagonal line indicating symmetry and the dashed line indicating equal g' .

of density ρ and the ambient fluid of density ρ_0 , defined by

$$g' \equiv g \frac{\rho - \rho_0}{\rho_0}, \quad (2)$$

190 where g is the gravitational acceleration. In the remainder of this
191 paper, g'_1 will be used refer to the reduced gravity of the current
192 with H_1 and ρ_1 , and g'_2 will be used to refer to the reduced gravity
193 of the current with H_2 and ρ_2 . In the experiments the values of
194 $g'_1, g'_2 < 30 \text{ cm s}^{-1}$ (Figure 2a), so that density differences are
195 less than 3%, and the flows can be considered as Boussinesq.

196 **Borden & Meiburg (2013)** provide an overview of Froude
 197 number predictions. Although there are different predictions of
 198 the Froude number, we use the expression by **Shin *et al.* (2004)**
 199 which is the only one that applies to both full-depth and partial-
 200 depth lock releases, and gives

$$F_H = \frac{\sqrt{2 - H/H_0}}{2}. \quad (3)$$

201 We note that the **Shin *et al.* (2004)** solution provides a closed-
 202 form analytic solution and is therefore based on a number of
 203 assumptions and physical simplifications. Numerical experiments
 204 may provide more detail on key physical processes. In the analysis
 205 of the results we assume the currents are two dimensional, and
 206 effects in the third lateral cross-channel dimension are ignored.

207 All experiments are mapped in parameter space in **Figure 2**.
 208 For the full-depth experiments (**Figure 2a**) the ratio of the reduced
 209 gravities of the lighter (g'_{light} = lower of g'_1 and g'_2) and the denser
 210 (g'_{heavy} = higher of g'_1 and g'_2) gravity currents,

$$r_g \equiv \frac{g'_{light}}{g'_{heavy}}, \quad (4)$$

211 ranged from $0.21 < r_g < 0.99$. For the half-depth experiments
 212 (**Figure 2b**) this ratio ranged from $0.19 < r_g < 0.97$.

213 3. Experimental results

214 Snapshots from two full-depth and half-depth experiments are
 215 shown in **Figures 3** and **4**, respectively. **Figure 3a** shows a
 216 symmetric case, where g'_{light} was almost equal to g'_{heavy} ($r_g =$
 217 0.99), **figure 3b** is a full-depth asymmetric case with the heavier
 218 fluid dyed blue (propagating from the right, $r_g = 0.33$). **Figure 4a**
 219 shows the collision between two currents with $r_g = 0.95$ but
 220 different heights, while in **Figure 4b** an experiment with two
 221 currents having approximately equal $g'H$ is shown (different g' ,
 222 different H). The associated videos are included as supplementary
 223 movies online.

224 The propagation of the gravity currents before collision
 225 (**Figures 3** and **4**, second row) will be discussed in **Section 3.1** and
 226 compared to the theoretical prediction (**Equation 3**). The collision
 227 will then be analysed in more detail. In particular, the shape and
 228 propagation speed of the collision front will be considered. Due to

mixing of the two dyed fluids and the ambient fluid upon collision, 229
 it is not possible to measure vertical velocities in the current 230
 experimental setup to a satisfactory accuracy, and these will hence 231
 not be discussed further. The shape of the collision front (**Figures 3** 232
 and **4**, third row) will be discussed from a qualitative standpoint. 233
 The maximum vertical displacement (**Figures 3** and **4**, fourth 234
 row) and the horizontal propagation speed of the collision front 235
 will be investigated quantitatively. The vertical displacements at 236
 the collision front will be discussed in **Section 3.2**. Horizontal 237
 propagation of the collision front and mixing along the collision 238
 front will be discussed **Section 3.3**. 239

240 3.1. Pre-collision gravity current propagation speed

The fronts of the gravity currents were observed to travel at 241
 a constant speed until they collided. **Figure 5** compares the 242
 measured Froude numbers of the gravity currents (**Equation 1**) 243
 with the theoretical prediction (**Equation 3**). The theoretical 244
 prediction for a dissipationless current (**Equation 3**) is plotted for 245
 both full-depth and half-depth lock heights (lines in **Figure 5**). 246
 Lower lock heights create slower propagating gravity currents 247
 with a higher Froude number. The observed Froude numbers are 248
 about 15% lower than the theoretical values, independent of the 249
 value of g' or the height H of the dense fluid in the lock, which is 250
 consistent with previous measurements of gravity current speeds 251
 (see e.g. the summary in **Shin *et al.* 2004**). For the full-depth 252
 experiments we find a mean Froude number of 0.42 instead of 253
 the theoretical prediction of 0.5. The mean Froude number for the 254
 half-depth experiments is 0.53, where theory predicts 0.61. These 255
 reductions from the predicted Froude numbers are mainly a result 256
 of energy loss associated with mixing with the ambient fluid due to 257
 shear instabilities along the top of the current (**Hughes & Linden** 258
2016) rather than frictional energy losses. 259

260 3.2. Collision shape and vertical displacement

Figure 6 shows the two collision events in **Figure 3** (third row) in 261
 more detail. Individual frames from the experimental videos were 262
 analysed to find the positions of the fronts in time. Depending on 263
 the shape of the front, rows or columns of pixels in the image 264
 were analysed using a threshold value of light intensity to find 265
 the front position. Both sequences start at time $\tau = 0$, which 266

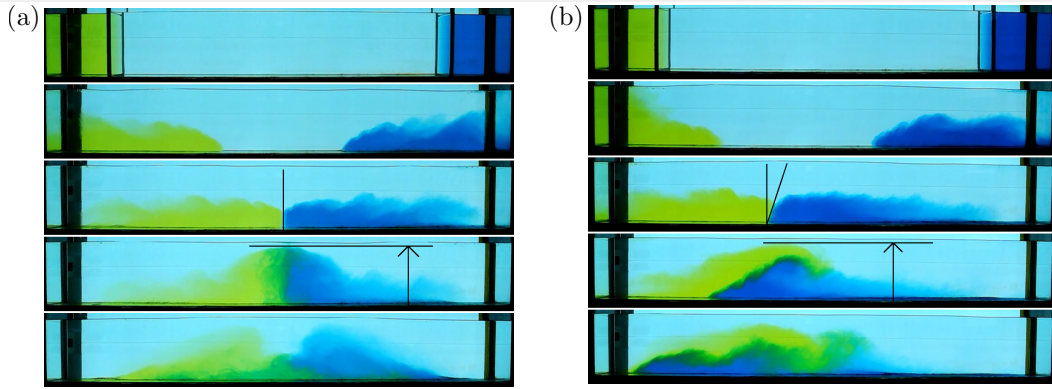


Figure 3. Snapshots of two full-depth experiments at different times. Note that the time difference between different panels is not the same for the two experiments. (a) symmetric case with $r_g = 0.99$, (b) asymmetric case with $r_g = 0.33$. Top: initial set-up, second row: pre-collision gravity currents, third row: initial collision, fourth row: maximum collision height, bottom: post-collision.

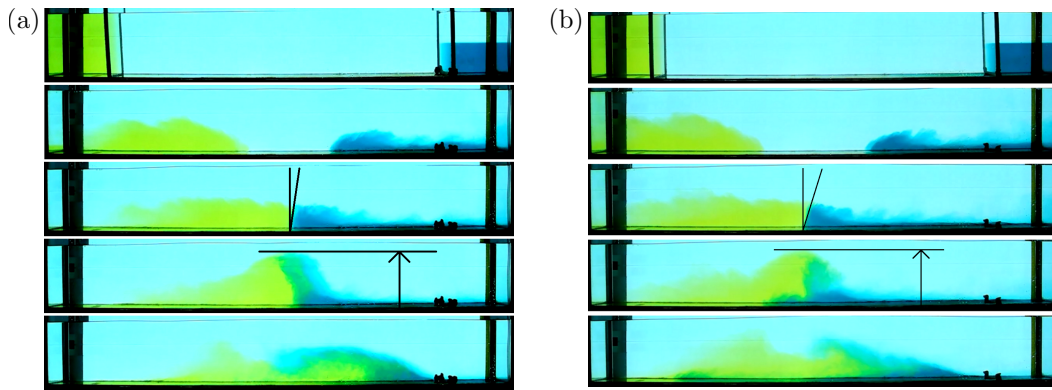


Figure 4. As Figure 3, but now for two half-depth experiments. (a) case with approximately equal g' ($r_g = 0.95$), (b) case with approximately equal $g'H$ ($r_g = 0.48$).

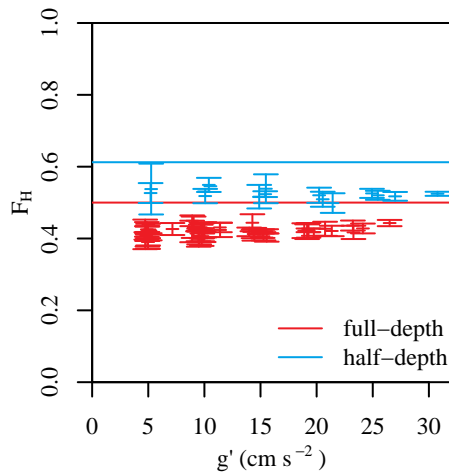


Figure 5. Froude numbers versus reduced gravity. Marks are individual experiments, lines are the theoretical values based on Equation 3. Error bars show the range of Froude numbers measured for each current. The red marks and line correspond to the full-depth experiments and blue marks and line to the half-depth experiments.

267 is the frame at which the fronts collide. Subsequent frames are
 268 separated by increments of 0.15 non-dimensional time units $\tau \equiv$
 269 $t/\sqrt{H_0/g'_1 + H_0/g'_2}$. The figures show a short period of time ($t =$
 270 1.3 s (a) and $t = 2.1$ s (b)) centered around the time corresponding
 271 to the third row of Figure 3. In the symmetric case horizontal rows
 272 were analyzed to locate the front position; therefore the top of the
 273 currents is not detected in the last four panels of Figure 6a.

In the symmetric case of equal g' (Figure 6a) the shapes of the
 274 individual gravity current fronts are essentially the same, and the
 275 collision front is vertical. In time this front extends in height and
 276 remains vertical. Mixing occurs along the collision line as can
 277 be seen by the presence of green dye resulting from the mixing
 278 of the blue and yellow dyes in the two currents. The asymmetric
 279 case is different (Figure 6b). The individual gravity current fronts
 280 change shape as they approach each other and therefore have
 281 different steepnesses upon collision. The collision front develops
 282 at an angle with the heavier dense fluid (blue, right) intruding
 283 underneath the lighter dense fluid (yellow, left). The front shape
 284 is not steady in time. At $\tau = 0.30$ a new gravity current forms
 285 at the bottom, and Kelvin-Helmholtz billows develop at the top
 286 of the denser (blue) current (Sha *et al.* 1991). The front shape
 287 evolves from an initial angled straight line to an 'S' shaped front
 288 that changes shape to become more horizontal with increasing
 289 time. The angle from the vertical at which the collision front forms
 290 (denoted in the third row of Figure 3 and at $\tau = 0.15$ in Figure 6)
 291 is zero for symmetric collisions (vertical front) and increases with
 292 increasing asymmetry between the colliding fronts (tilted front).
 293

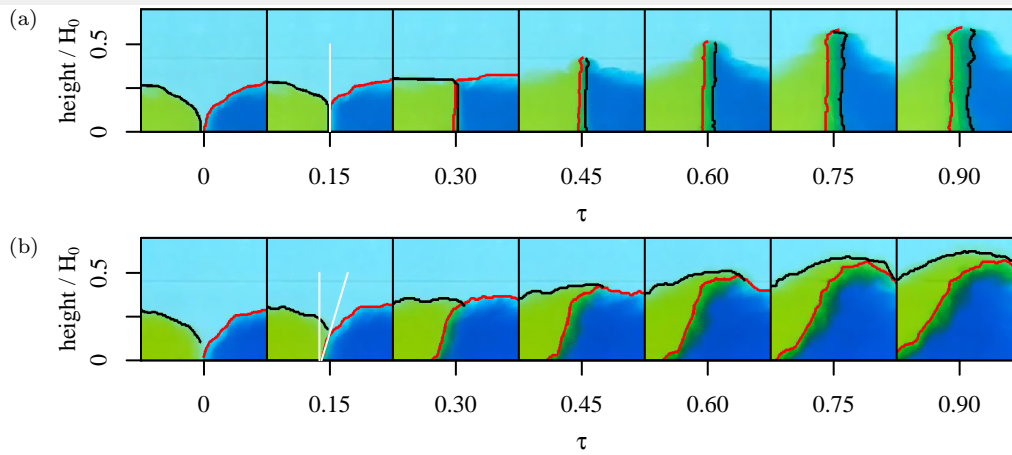


Figure 6. The front positions at and after collision for two different full-depth experiments. All heights are normalized by the total water depth, H_0 , and τ is the dimensionless time. These are the same experiments shown in Figure 3 with (a) $r_g = 0.99$ and (b) $r_g = 0.33$. The red line corresponds to the relatively heavier (blue) front and the black line to the lighter (yellow) front.

294 As a direct consequence of the ascending motions forced by
 295 the collision event, dyed fluid is displaced vertically. The energy-
 296 conserving theory of *Shin et al.* (2004) predicts that, before
 297 collision, the heights of the gravity currents is equal to half the
 298 lock depth, i.e.

$$h = \frac{1}{2}H_i, \quad i = 1, 2. \quad (5)$$

299 The heights of the individual gravity currents from full-depth
 300 lock releases (blue and purple marks in Figure 7a and purple
 301 marks in Figure 7b) agree with these theoretical values (blue and
 302 purple lines in Figure 7a and purple line in Figure 7b). There is
 303 a discrepancy between the measured and predicted height of the
 304 current for the half-depth lock releases. This discrepancy may be
 305 caused by the limited length of the lock in the current experimental
 306 setup or by the assumptions that were made in the theoretical
 307 model. Further experiments with a numerical model could be used
 308 to investigate the cause of the difference between experiment and
 309 theory.

310 After collision, the maximum height of the dyed fluids in the
 311 full-depth experiments is approximately 0.90 of the total water
 312 depth, independent of r_g (red marks in Figure 7a) or pre-collision
 313 propagation speeds (not shown). The half-depth experiments
 314 (Figure 7b) show more variation in collision height, although
 315 no systematic trends can be inferred. Despite there being two
 316 significantly different lifting processes, the maximum collision
 317 height is observed to be comparable, independent of the dominant
 318 lifting process.

319 Based on the small spread of maximum heights in the data and
 320 the corresponding error bars, it is difficult to determine the role of

gravity current height, density and speed. For all experiments the
 maximum height of the fluid raised in the collision is a significant
 fraction of the total fluid depth, and it is possible that the presence
 of the free surface has an influence on the vertical motion near the
 top of the rising dense fluid.

3.3. Horizontal propagation of the collision front

326 Figures 3a and 6a show that in the full-depth symmetric case
 327 the collision front is stationary. There is some mixing, but the
 328 front does not move horizontally from the point of impact.
 329 In the asymmetric case the heavier gravity current (dyed blue,
 330 propagating from the right) continues propagating in its original
 331 direction (Figures 3b and 6b). In Figure 8, Hovmöller diagrams for
 332 three full-depth experiments are shown. These have been created
 333 by selecting a horizontal line one pixel thick along the bottom
 334 of the tank and stacking consecutive frames. The colour in these
 335 figures is the same as in Figures 3 and 6. The constant speeds of
 336 the two fronts before collision are shown by the straight edges
 337 to the yellow and blue regions at early times. The speeds of the
 338 individual currents essentially do not change prior to the point of
 339 impact.

340 The symmetric case confirms earlier observations; the
 341 individual gravity currents propagate at equal speeds toward each
 342 other, and upon collision mixing occurs. There is no evidence of
 343 further horizontal propagation of the collision front, and a growing
 344 mixed region develops between the now stationary currents, as can
 345 be seen from the green striated region from $t > 5$ s in Figure 8a. In
 346 the strongly asymmetric case (Figure 8b, $r_g = 0.33$) the heavier
 347

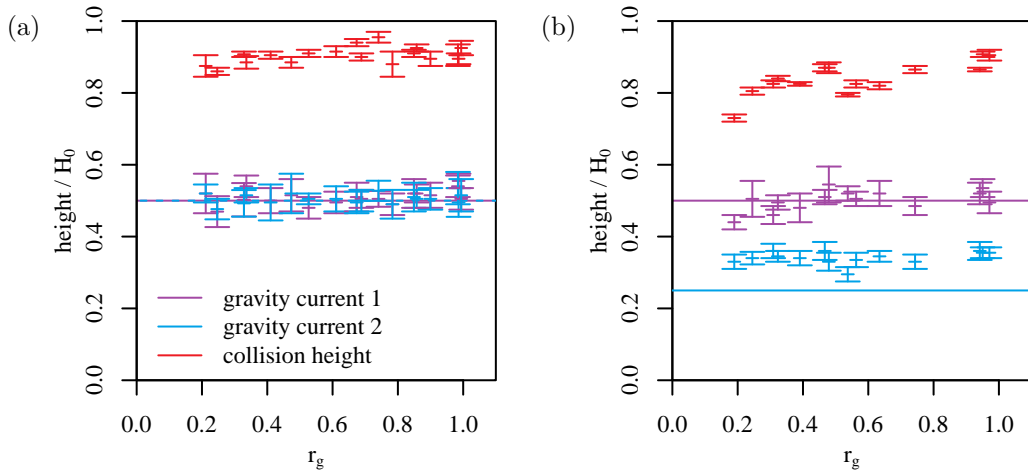


Figure 7. Pre-collision gravity current heights (blue and purple symbols) and maximum height (red symbols) reached after collision against ratio r_g . All heights are normalized by the total water depth, H_0 . The horizontal lines show the theoretical, energy conserving value for the height of a gravity current. Error bars show the range of measured maximum heights for each experiment. (a) Full-depth experiments and (b) half-depth experiments in the same colours.

348 current (dyed blue, propagating from the right) continues to
 349 propagate in the same direction with a slightly reduced speed
 350 after collision. The flow of the lighter (yellow) current above the
 351 heavier (blue) current is not captured in this plot. Again there
 352 is mixing along the collision front that increases with time after
 353 impact. A third experiment with a weaker asymmetry ($r_g = 0.61$)
 354 is shown in Figure 8c. Similar to the previous experiment, the
 355 collision front propagates in the direction of the propagation of the
 356 heavier current, but in this case the heavier (blue, right) current is
 357 significantly slower after collision. The mixing along the front of the
 358 heavier current is greater, as inferred from the size of the green
 359 region, than in the more strongly asymmetric case (Figure 8b).

360 The horizontal propagation speed of the heavier current after
 361 collision has been measured for all full-depth experiments. In
 362 Figure 9 these measured post-collision front speeds are plotted
 363 against the characteristic speed associated with the density
 364 difference between the two currents:

$$\sqrt{g'_c H_0}, \quad (6)$$

365 with the reduced gravity g'_c based on the densities of the two
 366 interacting currents:

$$g'_c = g \frac{\rho_{heavy} - \rho_{light}}{\rho_0}. \quad (7)$$

367 The near-symmetric collisions ($r_g > 0.89$, blue marks in
 368 Figure 9) create stationary fronts, as can also be seen in Figures 3a,

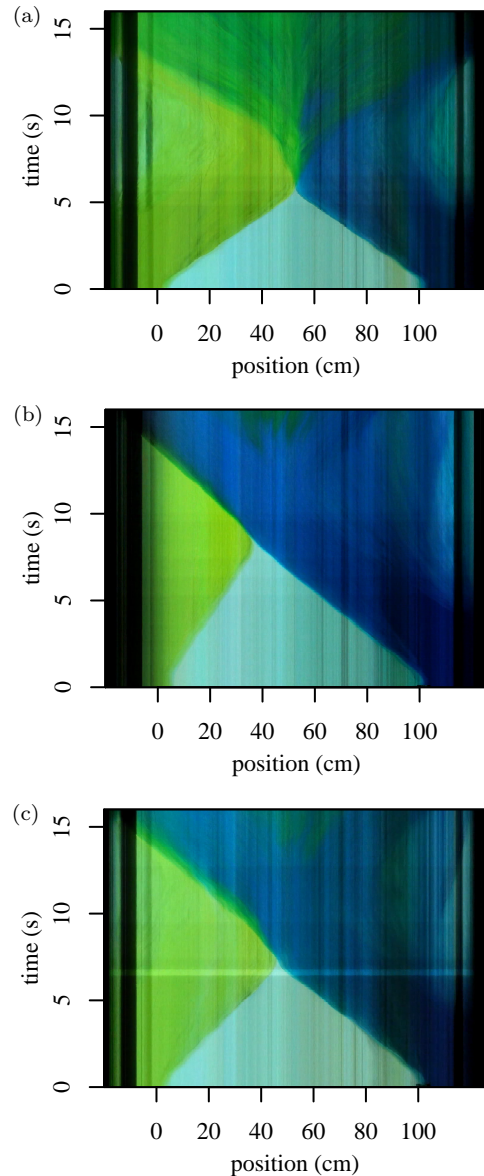


Figure 8. Hovmöller diagrams for three full-depth experiments. Two of the experiments are the same as shown in Figures 3 and 6 with (a) $r_g = 0.99$, (b) $r_g = 0.33$ and (c) $r_g = 0.61$.

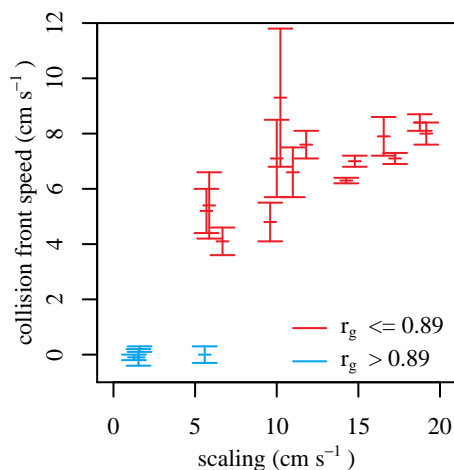


Figure 9. Experimental collision speed versus a simple scaling (Equation 6, cm s^{-1}) for the full-depth experiments. Marks are the individual experiments. Error bars show the range of measured front speeds for each collision front. Blue marks correspond to symmetric collisions ($r_g > 0.89$), red marks correspond to the most asymmetric collisions ($r_g \leq 0.89$).

369 6a and 8a. However, the characteristic speed (Equation 6) is low
 370 but positive for these cases, indicating slow propagation of the
 371 collision front, while mixing along the collision front reduces
 372 density differences and prevents horizontal propagation.

373 For the asymmetric collisions ($r_g \leq 0.89$, red marks in
 374 Figure 9) the collision front propagates in the same direction as
 375 that of the heavier current. The speed of propagation lies between
 376 4 and 9 cm s^{-1} and increases with asymmetry of the collision
 377 and with increasing value of the characteristic speed given by
 378 Equation 6. A model describing this post collision propagation
 379 should include the effects of the dynamics of the gravity currents
 380 before collision, the effects of mixing and the density difference
 381 at collision. Attempts to derive such a model using the formalism
 382 explored by Shin *et al.* (2004) have been unsatisfactory.

383 The post-collision phase is very different in the half-depth
 384 experiments, as may be noted in the snapshots of Fig. 4. In
 385 the case of equal g' , the collision front is nearly vertical at the
 386 moment of impact, but soon after the higher current (dyed yellow,
 387 travelling from the left) pushes back the lower current (dyed blue,
 388 travelling from the right, Fig. 4a). This is in contrast with the
 389 full-depth symmetric experiment in which the collision front is
 390 stationary (Fig. 3a). The collision event for two currents of equal
 391 $g'H$ ($r_g = 0.48$) also differs from the full-depth experiments:
 392 upon impact the collision front is tilted, in a similar way to that
 393 observed in the full-depth experiments. Afterwards, a part of the
 394 heavier but lower current (dyed blue, propagating from the right)
 395 forms a new current and propagates onwards into the fluid from

the other current, again as observed in the asymmetric full-depth 396
 experiments. However, part of the heavier but lower current is 397
 pushed back by the lighter fluid that after rising vertically, sinks 398
 and continues propagating in its original direction. 399

The collision front is not well-defined in the half-depth 400
 experiments because of the motions generated by the lighter but 401
 higher current. For this reason, we do not extend the post-collision 402
 propagation analysis to these experiments. 403

4. Conclusions 404

Experiments using gravity currents to model two-dimensional sea 405
 and land breeze collisions have been performed. Two gravity 406
 currents were generated from a lock-release and allowed to collide 407
 in a rectangular channel. Both the density and the height of the 408
 currents were varied in the different experiments. 409

Before collision, the gravity currents propagate with a constant 410
 Froude number about 15% lower than energy conserving theory 411
 predicts, as previous studies have also shown (e.g. Shin *et al.* 412
 2004). At collision a sharp front between the two currents 413
 develops. For a collision of two similar currents ($r_g \approx 1.0$, equal 414
 heights) the front is vertical and does not move horizontally. With 415
 increasing asymmetry the front is no longer vertical but instead 416
 tilts, with the heavier gravity current propagating underneath 417
 the lighter current. The front is not steady; over time a new 418
 gravity current develops, and the collision front propagates in 419
 the same direction of the original heavier current. Mixing along 420
 the collision front decreases with asymmetry: more asymmetrical 421
 currents (lower r_g) show less mixing. The maximum height 422
 reached by the dense fluids during collision is significantly above 423
 the height of the two individual gravity currents. The collision 424
 front is less clear for two currents having different lock heights, 425
 and the higher gravity current sets the direction of post-collision 426
 propagation. 427

In the natural environment, sea breeze circulations or 428
 convective outflows are influenced by multiple factors, and 429
 their collisions are therefore complex. These experiments were 430
 designed to give physical insights into the dynamics of the 431
 collisions, which are difficult to measure in detail in nature. 432
 Wilson *et al.* (1998) note that for the initiation and maintenance 433
 of convection along a front, continuous strong ascending 434

435 motions in the location of the developing storm are important.
 436 In the experiments, the two gravity current fronts interact,
 437 and their shapes change dramatically upon collision. There is
 438 significant ascent along the collision front, resulting in the
 439 vertical displacement of gravity current fluid. These vertical
 440 displacements have been found in all collision events and, in
 441 the natural environment, could provide the necessary trigger to
 442 overcome the convective inhibition (i.e. reach levels of positive
 443 buoyancy), setting off deep convective motions. More symmetric
 444 collisions have greater potential for initiating or enhancing deep
 445 convective motions because the horizontal position of the ascent
 446 is stationary. In the absence of ambient wind this would create
 447 more favourable conditions for developing deep convection than
 448 the asymmetric case, where the collision front propagates and the
 449 convective forcing changes position constantly. However, even in
 450 asymmetric collisions convection may be initiated if the lighter
 451 fluid is displaced vertically above its level of free convection.

452 In the current experimental setup the strength of vertical
 453 motions and mixing ratios could not be quantified. A new
 454 set of experiments (laboratory or numerical) could therefore
 455 provide valuable additional data. Further work might examine
 456 the energetics of kinetic and potential energy transformations
 457 during the collisions in more detail. Furthermore, the experiments
 458 could be extended to investigate gravity currents collision in a
 459 radially-symmetric setup (as in [Slim & Huppert 2004](#)), relevant
 460 for the collision of sea breezes over (near) circular islands. Future
 461 analysis may aim to provide a description for the post-collision
 462 horizontal propagation speeds as measured in the experiments.
 463 In nature, and in the experiments, the post-collision motions
 464 also involve reflected waves and bores, as discussed by [Simpson](#)
 465 (1997) and [Shin \(2001\)](#), and as can be seen in Figure 3. We have
 466 chosen to concentrate on the initial collision front here, but these
 467 other aspects would be worth further study.

468

469 Acknowledgements

470 The authors gratefully acknowledge the National Science
 471 Foundation (Grant OCE- 0824636) and the Office of Naval
 472 Research (Grant N00014-09-1-0844) for their support of the 2013
 473 WHOI Geophysical Fluid Dynamics Summer School where much

of the research presented in this paper was performed. The authors
 thank Anders Jensen for the able assistance in setting up the
 laboratory experiments. STG also acknowledges support from the
 National Aeronautics and Space Administration (Grant NASA
 NNX14A078G).

Supplementary materials

Supplementary movies are available online.

References

- Arritt, R W. 1993. Effects of the large-scale flow on characteristic features of
 the sea breeze. *Journal of Applied Meteorology*, **32**(1), 116–125.
- Baker, R David, Lynn, Barry H, Boone, Aaron, Tao, Wei-Kuo, & Simpson,
 Joanne. 2001. The influence of soil moisture, coastline curvature, and
 land-breeze circulations on sea-breeze-initiated precipitation. *Journal of*
Hydrometeorology, **2**(2), 193–211.
- Banacos, Peter C, & Schultz, David M. 2005. The use of moisture flux
 convergence in forecasting convective initiation: Historical and operational
 perspectives. *Weather and Forecasting*, **20**(3), 351–366.
- Blanchard, D O, & López, Raúl E. 1985. Spatial patterns of convection in
 south Florida. *Monthly Weather Review*, **113**(8), 1282–1299.
- Borden, Z, & Meiburg, E. 2013. Circulation based models for Boussinesq
 gravity currents. *Physics of Fluids*, **25**(101301), 1 – 14.
- Britter, RE, & Simpson, JE. 1978. Experiments on the dynamics of a gravity
 current head. *Journal of Fluid Mechanics*, **88**(02), 223–240.
- Browning, K A, Blyth, A M, Clark, P A, Corsmeier, U, Morcrette, C J,
 Agnew, J L, Ballard, S P, Bamber, D, Barthlott, C, Bennett, L J, *et al.* .
 2007. The Convective Storm Initiation Project. *Bulletin of the American*
Meteorological Society, **88**(12).
- Burpee, R W. 1979. Peninsula-scale convergence in the south Florida sea
 breeze. *Monthly Weather Review*, **107**(7), 852 – 860.
- Byers, H R, & Rodebush, H R. 1948. Causes of thunderstorms of the Florida
 peninsula. *Journal of Meteorology*, **5**(6), 275–280.
- Carbone, R E, Conway, J W, Crook, N A, & Moncrieff, M W. 1990. The
 generation and propagation of a nocturnal squall line. Part I: Observations
 and implications for mesoscale predictability. *Monthly Weather Review*,
118(1), 26–49.
- Carbone, R E, Wilson, J W, Keenan, T D, & Hacker, J M. 2000. Tropical
 island convection in the absence of significant topography. Part I: Life cycle
 of diurnally forced convection. *Monthly Weather Review*, **128**(10), 3459–
 3480.
- Cenedese, C, & Adduce, C. 2008. Mixing in a density-driven current flowing
 down a slope in a rotating fluid. *Journal of Fluid Mechanics*, **604**, 369–388.
- Clarke, R H. 1983. Fair weather nocturnal inland wind surges and atmospheric
 bores. Part I: Nocturnal wind surges. *Australian Meteorological Magazine*,
31, 133–45.

- 518 Crook, N A. 2001. Understanding Hector: The dynamics of island
519 thunderstorms. *Monthly Weather Review*, **129**(6), 1550–1563.
- 520 Dai, Albert. 2013. Experiments on gravity currents propagating on different
521 bottom slopes. *Journal of Fluid Mechanics*, **731**, 117–141.
- 522 Droegemeier, K K, & Wilhelmson, R B. 1985. Three-dimensional numerical
523 modeling of convection produced by interacting thunderstorm outflows.
524 Part II: Variations in vertical wind shear. *Journal of the atmospheric
525 sciences*, **42**(22), 2404–2414.
- 526 Fankhauser, JC, Crook, NA, Tuttle, J, Miller, LJ, & Wade, CG. 1995.
527 Initiation of deep convection along boundary layer convergence lines in a
528 semitropical environment. *Monthly weather review*, **123**(2), 291–314.
- 529 Forbes, Gregory S, & Merritt, Jonathan H. 1984. Mesoscale vortices over the
530 Great Lakes in wintertime. *Monthly weather review*, **112**(2), 377–381.
- 531 Gahmberg, M, Savijrvi, H, & Leskinen, M. 2010. The influence of synoptic
532 scale flow on sea breeze induced surface winds and calm zones. *Tellus*,
533 **62**(2), 209–217.
- 534 Gille, S T, & Llewellyn Smith, S G. 2014. When land breezes collide:
535 Converging diurnal winds over small bodies of water. *Quarterly Journal of
536 the Royal Meteorological Society*. published online, doi: 10.1002/qj.2322.
- 537 Gille, S T, Llewellyn Smith, S G, & Lee, S M. 2003. Measuring the sea breeze
538 from QuikSCAT scatterometry. *Geophysical Research Letters*, **30**(3), 1114.
- 539 Golding, B. 2005. *Boscastle and North Cornwall Post Flood Event Study
540 - Meteorological Analysis of the Conditions Leading to Flooding on 16
541 August 2004*. Tech. rept. 459. Met Office, UK.
- 542 Hacker, J, Linden, PF, & Dalziel, SB. 1996. Mixing in lock-release gravity
543 currents. *Dynamics of Atmospheres and Oceans*, **24**(1), 183–195.
- 544 Helmis, CG, Asimakopoulos, DN, Deligiorgi, DG, & Lalas, DP. 1987.
545 Observations of sea-breeze fronts near the shoreline. *Boundary-Layer
546 Meteorology*, **38**(4), 395–410.
- 547 Hughes, G. O., & Linden, P. F. 2016. Mixing efficiency in run-down gravity
548 currents. *J. Fluid Mech.*
- 549 Kingsmill, D E. 1995. Convection initiation associated with a sea-breeze front,
550 a gust front, and their collision. *Monthly Weather Review*, **123**(10), 2913–
551 2933.
- 552 Mangia, Cristina, Martano, Paolo, Miglietta, Mario Marcello, Morabito,
553 Angela, & Tanzarella, Annalisa. 2004. Modelling local winds over the
554 Salento peninsula. *Meteorological Applications*, **11**(3), 231–244.
- 555 Mangia, Cristina, Schipa, Ilenia, Tanzarella, Annalisa, Conte, Dario, Marra,
556 Gian Paolo, Marcello Miglietta, Mario, & Rizza, Umberto. 2010. A
557 numerical study of the effect of sea breeze circulation on photochemical
558 pollution over a highly industrialized peninsula. *Meteorological
559 Applications*, **17**(1), 19–31.
- 560 Maxworthy, T, Leilich, JSJE, Simpson, JE, & Meiburg, EH. 2002. The
561 propagation of a gravity current into a linearly stratified fluid. *Journal of
562 Fluid Mechanics*, **453**, 371–394.
- 563 Miller, S T K, Keim, B D, Talbot, R W, & Mao, H. 2003. Sea breeze: structure,
564 forecasting, and impacts. *Reviews of Geophysics*, **41**, 1–31.
- Moncrieff, M W, & Liu, C. 1999. Convection initiation by density currents: 565
Role of convergence, shear, and dynamical organization. *Monthly Weather* 566
Review, **127**(10), 2455–2464. 567
- Nicholls, M E, Pielke, R A, & Cotton, W R. 1991. A two-dimensional 568
numerical investigation of the interaction between sea breezes and deep 569
convection over the Florida peninsula. *Monthly Weather Review*, **119**(2), 570
298–323. 571
- Niino, H. 1987. The linear theory of land and sea breeze circulation. *Journal* 572
of the Meteorological Society of Japan, **65**(6), 901–921. 573
- Niziol, Thomas A, Snyder, Warren R, & Waldstreicher, Jeff S. 1995. Winter 574
weather forecasting throughout the eastern United States. Part IV: Lake 575
effect snow. *Weather and Forecasting*, **10**(1), 61–77. 576
- Noonan, J A, & Smith, R K. 1986. Sea-breeze circulations over Cape York 577
Peninsula and the generation of Gulf of Carpentaria cloud line disturbances. 578
Journal of the Atmospheric Sciences, **43**(16), 1679–1693. 579
- Pielke, R A. 1974. A three-dimensional numerical model of the sea breezes 580
over south Florida. *Monthly Weather Review*, **102**(2), 115–139. 581
- Ramis, C, Jansá, A, & Alonso, S. 1990. Sea breeze in Mallorca. A numerical 582
study. *Meteorology and Atmospheric Physics*, **42**(3-4), 249–258. 583
- Rizza, Umberto, Miglietta, Mario Marcello, Anabor, Vagner, Degrazia, 584
Gervasio A, & Maldaner, Silvana. 2015. Large-eddy simulation of sea 585
breeze at an idealized peninsular site. *Journal of Marine Systems*, **148**, 586
167–182. 587
- Robinson, FJ, Patterson, Michael D, & Sherwood, SC. 2013. A Numerical 588
Modeling Study of the Propagation of Idealized Sea-Breeze Density 589
Currents. *Journal of the Atmospheric Sciences*, **70**(2), 653–668. 590
- Rottman, J W, & Simpson, J E. 1983. Gravity currents produced by 591
instantaneous releases of a heavy fluid in a rectangular channel. *Journal* 592
of Fluid Mechanics, **135**, 95–110. 593
- Sha, Weiming, Kawamura, Takeshi, & Ueda, Hiromasa. 1991. A numerical 594
study on sea/land breezes as a gravity current: Kelvin-Helmholtz billows 595
and inland penetration of the sea-breeze front. *Journal of the atmospheric* 596
sciences, **48**(14), 1649–1665. 597
- Shin, J O. 2001. *Colliding gravity currents*. Ph.D. thesis, University of 598
Cambridge. 599
- Shin, J O, Dalziel, S B, & Linden, P F. 2004. Gravity currents produced by 600
lock exchange. *Journal of Fluid Mechanics*, **521**, 1–34. 601
- Simpson, J E. 1997. Gravity Currents in the Environment and the Laboratory. 602
Journal of Fluid Mechanics, **352**, 376–378. 603
- Simpson, J E, Mansfield, D A, & Milford, J R. 1977. Inland penetration of 604
sea-breeze fronts. *Quarterly Journal of the Royal Meteorological Society*, 605
103(435), 47–76. 606
- Simpson, JE. 1969. A comparison between laboratory and atmospheric density 607
currents. *Quarterly Journal of the Royal Meteorological Society*, **95**(406), 608
758–765. 609
- Slim, Anja C, & Huppert, Herbert E. 2004. Self-similar solutions of 610
the axisymmetric shallow-water equations governing converging inviscid 611

- 612 gravity currents. *Journal of Fluid Mechanics*, **506**, 331–355.
- 613 Soderholm, Joshua, McGowan, Hamish, Richter, Harald, Walsh, Kevin,
614 Weckwerth, Tammy, & Coleman, Matthew. 2015. The Coastal Convective
615 Interactions Experiment (CCIE): Understanding the role of sea breezes
616 for hailstorm hotspots in Eastern Australia. *Bulletin of the American*
617 *Meteorological Society*.
- 618 Sumner, Graham, Ramis, Clemente, & Guijarro, José A. 1993. The spatial
619 organization of daily rainfall over Mallorca, Spain. *International Journal*
620 *of Climatology*, **13**(1), 89–109.
- 621 Tijm, A B C, van Delden, A J, & Holtslag, A A M. 1999. The Inland
622 Penetration of Sea Breezes. *Contributions to Atmospheric Physics*, **72**, 317–
623 328.
- 624 Wapler, Kathrin, & Lane, Todd P. 2012. A case of offshore convective
625 initiation by interacting land breezes near Darwin, Australia. *Meteorology*
626 *and Atmospheric Physics*, **115**(3-4), 123–137.
- 627 Warren, R A. 2014. *Quasi-stationary Convective Systems in the UK*. Ph.D.
628 thesis, University of Reading.
- 629 Wilson, J W, Crook, N A, Mueller, C K, Sun, J, & Dixon, M. 1998. Nowcasting
630 thunderstorms: a status report. *Bulletin of the American Meteorological*
631 *Society*, **79**(10), 2079–2099.
- 632 Wilson, James W, & Schreiber, Wendy E. 1986. Initiation of convective storms
633 at radar-observed boundary-layer convergence lines. *Monthly Weather*
634 *Review*, **114**(12), 2516–2536.
- 635 Wulfmeyer, V, Behrendt, A, Kottmeier, C, Corsmeier, U, Barthlott, C, Craig,
636 G C, Hagen, M, Althausen, D, Aoshima, F, Arpagaus, M, *et al.* . 2011.
637 The Convective and Orographically-induced Precipitation Study (COPS):
638 The scientific strategy, the field phase, and research highlights. *Quarterly*
639 *Journal of the Royal Meteorological Society*, **137**(S1), 3–30.
- 640 Xian, Z, & Pielke, R A. 1991. The effects of width of landmasses on the
641 development of sea breezes. *Journal of Applied Meteorology*, **30**(9), 1280–
642 1304.
- 643 Yan, H, & Anthes, R A. 1987. The effect of latitude on the sea breeze. *Monthly*
644 *Weather Review*, **115**(5), 936–956.